Soft Matter

ARTICLE TYPE

Cite this: DOI: 10.1039/xxxxxxxxxx

A quantitative study of the effect of flow on the photopolymerization of fibers†

Malcolm Slutzky,[a] Howard A. Stone,[b] and Janine K. Nunes*[b]

Received Date
Accepted Date

DOI: 10.1039/xxxxxxxxxx

www.rsc.org/journalname

Pulsed-UV light in the continuous flow of a photo-crosslinkable liquid can result in gelation and is a useful method to produce soft microfibers with uniform sizes. With modeling and experiments, we characterize some aspects of this fiber fabrication process. We model the spatial concentration profiles of radical species and molecular oxygen in the flow direction during light exposure, and predict the critical conditions for the onset of fiber formation and compare these predictions with experimental observations. We also characterize the different regimes of microfiber production (no polymerization, non-uniform fibers, and uniform microfibers), qualitatively characterize the rigidity of the fibers, and demonstrate that we can predictably control the length of the produced microfibers for a range of process parameters.

1 Introduction

Gel microfibers are a promising class of high aspect ratio soft materials that can possess a growing range of properties and functionalities, including complex micro-architectures and microcompartmentalization,[1–3] a broad range of mechanical properties including tunable elasticity,[4] stimuli-responsiveness,[5] and the ability to encapsulate and deliver different materials.[1,6] These properties make the microfibers valuable in the biomedical and materials science fields, for example, as scaffolds for tissue engineering,[7] micromotors,[8] and as rheological modifiers and gelling agents.[9]

Microfluidics offers a versatile platform for precise and uniform flow control at the microscale that can be harnessed to precisely control the uniform generation of microscale objects. Continuous-flow gelation microfluidic techniques have emerged as versatile strategies for producing gel microfibers and other gel micro-objects.[10–17] Among these techniques, some involve the use of UV light to convert a flowing photo-crosslinkable liquid to a gel, such as in a photoinitiated free radical polymerization reaction.[11] The kinetics of such free radical polymerization reactions have been studied extensively, both in bulk and thin films.[18–21] In addition, kinetic models have been developed for microfluidic systems with a stationary reactive liquid phase,[22] as well as flowing reactive droplet phases.[23]

Typically, a microfiber can be produced as one continuous object, collected either randomly or spooled.[7,24] This fiber can then be mechanically cut into shorter fibers post-fabrication, for example, using a cryo-sectioning technique,[25] or they can be formed with the desired lengths in situ. A few microfluidic approaches that have been developed for generating uniform length microfibers in situ include the use of valves,[1,26] bubbles,[27,28] and light.[9,17] We have previously used pulses of UV light to gel a jet of photo-crosslinkable solution to form suspensions of microfibers with uniform lengths.[9] Others have recently compared the generation of rods and fibers by continuous UV illumination of plugs and pulsed UV illumination of jets, respectively.[17] Here, we consider more quantitatively this process of fiber formation, since the relationships among process parameters and specific fiber properties are relatively unexplored. Not only does this lack of knowledge limit the applicability of gel microfibers, it also impacts our ability to scale up this fiber production process, as it is still unclear how well the microfiber properties can be effectively predicted and controlled.

The precise length control provided by pulsed-light continuous-flow gelation allows for fiber batches to be produced with greater uniformity, a necessary step for the more widespread use of these microfibers in various applications. In situations where a high degree of fiber standardization is required, such as in the mass-production of uniform fibers, this technique's in situ length control provides a direct path from the production of polymerized material to the collection of the final product, leaving less room for mechanical error.

In this paper, we seek to characterize microfibers fabricated by continuous-flow gelation by studying the relationships between experimental conditions and fiber properties, such as length, width, and (qualitatively) rigidity. By modeling the chemical processes involved in the fiber production, and then comparing the

[a] Department of Physics, Princeton University, Princeton, NJ, 08544, USA.
[b] Department of Mechanical and Aerospace Engineering, Princeton University, Princeton, NJ, 08544, USA. E-mail: hastone@princeton.edu; nunes@princeton.edu.

† Electronic Supplementary Information (ESI) available: additional experimental graphs. See DOI: 10.1039/cXsm00000x/

This journal is © The Royal Society of Chemistry [year]

predictions to our experimentally-observed results, we can anticipate the properties of fibers produced with a given set of experimental conditions and provide general guidelines for standardized fiber production.

2 Experimental Procedure

The microfluidic device was fabricated using maskless direct-write lithography and soft lithography processes.[29] Briefly, a silicon wafer was coated with a thin layer of SU-8 2075 photoresist (MicroChem), using a standard spin coating and pre-bake procedure. The design of the microfluidic device was then exposed onto the photoresist-coated wafer with light of wavelength 375 nm, using a laser writer (Heidelberg microPG 101). Following exposure, standard post-exposure bake and developing procedures were used to finish fabrication of the master mold. The master was then silanized with chlorotrimethylsilane to prepare it for polydimethylsiloxane (PDMS, Dow Corning Sylgard 184) molding. Individual PDMS devices were cut from the mold, and biopsy punches were used to create 1 mm inlet holes and 2 mm outlet holes for each device. Larger outlet holes were utilized to allow more space for rigid fibers to exit the device without breaking. Glass slides were spin coated with a thin layer of PDMS and heated for at least 2 hours at 90 °C, in order to cure the PDMS layer. These coated slides were then bonded to the exposed PDMS channels using a Corona Surface Treater (Electro-Technic Products) and left at 95 °C for at least an hour. Finally, they were transferred to a 65 °C oven for at least 2 days to finish the bonding process and ensure hydrophobic devices.

The oligomer solution was prepared with, by volume, 54% poly (ethylene glycol) diacrylate (PEG-DA, molecular weight = 575 g/mol), 37% de-ionized water, 5% dye solution (20 mg/ml acryloxyethyl thiocarbamoyl rhodamine B, Polysciences, in dimethyl sulfoxide), and 4% 2-hydroxy-2-methylpropiophenone (photoinitiator, P_i). The oil solution was prepared with, by mass, 62% heavy mineral oil (Fisher Scientific), 27% hexadecane, and 11% Span 80. The viscosity of the oligomer solution was approximately 16 mPa-s, and the viscosity of the oil solution was approximately 35 mPa-s, measured with a rheometer (Anton Paar MCR 301). Chemicals were obtained from Sigma-Aldrich unless otherwise stated.

The fiber fabrication set-up consisted of an ultraviolet light-emitting diode (UV LED) with a mounted 20× focusing objective, a slide holder mounted on a 3-axis linear stage, and a UV-enhanced CCD camera (all purchased from Thorlabs), as shown in Figure 1. A mask, with a small slit 2.3 mm wide, was taped to the glass slide of the device to ensure no fluid upstream of the stable jet region was exposed to UV light, and which fixed the UV spot size $L = 2.3$ mm. The device was secured to the experimental set-up and positioned, with the use of the camera, so that the UV spot was centered over the entire width of the channel, $w_2 = 200\ \mu$m; the channel height $H = 135\ \mu$m.

The UV light intensity from the LED was controlled by varying the current. We calibrated the LED for different current settings by measuring the light power output at the focusing objective with an optical power meter and silicon photodiode power sensor (Thorlabs). To estimate the area of the UV light spot, we exposed a thin film of the oligomer solution and measured the polymerized spot size. In this paper, we report intensity in moles of photons per area per time (E/(m^2 s)), given that the energy in a mole of photons (Einstein, E) is Nhc/λ, where N is Avogadro's number, h is Planck's constant, c is the speed of light, and λ is the wavelength of light.[30] *Safety note:* The UV LED radiates intense UV light (output power greater than 1.15 W), so UV laser safety glasses were worn at all times during operation.

At the focusing junction in the microfluidic device, two symmetric streams of oil solution focused and sheathed the central stream of oligomer solution forming a uniform cylindrical jet that extended several millimeters downstream in the main channel before breaking up into droplets, as illustrated in Figure 1. Two syringe pumps (Harvard Apparatus) were used to control the oligomer flow rate Q_1 and oil flow rate Q_2, with $Q_2/Q_1 = 7.5$ to produce approximately the same oligomer jet diameter, $w_1 \approx 40\ \mu$m, for all experiments. After allowing the flows to stabilize, UV light of average wavelength 365 nm was focused on the stable uniform region of the jet and pulsed in regular intervals with a desired intensity, creating cylindrical fibers of identical length, diameter, and mechanical properties. The time between pulses was kept at 50 ms for all experiments. The oil solution, oligomer solution, and produced fibers were collected in petri dishes after flowing out of the outlet tubing and then observed under a microscope (Leica DMI4000B). Fiber diameters and lengths were measured using the Leica Application Suite while qualitative characterization of the fibers was observed. For a given sample, 5 fibers were measured to establish the sample's average length. The typical standard deviation of fiber lengths measured within a sample was less than 2% of the average length within a sample, except for fibers created in the transitional regime (discussed in Section 4), where the typical standard deviation was found to be approximately 5% of the average fiber length.

Before presenting the experimental results in Section 4, we discuss a model of the photopolymerization chemistry in flow, and corresponding predictions for the critical conditions for fiber formation.

3 Steady-state flow model of photopolymerization

In this section, we present the equations describing the steady-state distribution of chemical species involved with the photopolymerization from a fixed light source shining on a flowing oligomeric solution, which contains a photoinitiator. A photopolymerization reaction scheme, with simplified reaction steps I-V, is shown in Table 1.[18,22] We follow standard models of photopolymerization and the role of oxygen as a quencher of free radicals that drive polymerization (e.g., Dendukuri et al.[22] who studied time-dependent photopolymerization for stop-flow lithography).

Here we assume that the central aqueous stream containing oligomer and photoinitiator flows with uniform speed U. The oligomer of interest is multifunctional, having two or more carbon-carbon double bonds per molecule; during photopolymerization, the oligomer crosslinks to form a gel, i.e., undergoes gelation. The concentration of unreacted double bonds in the

This journal is © The Royal Society of Chemistry [year]

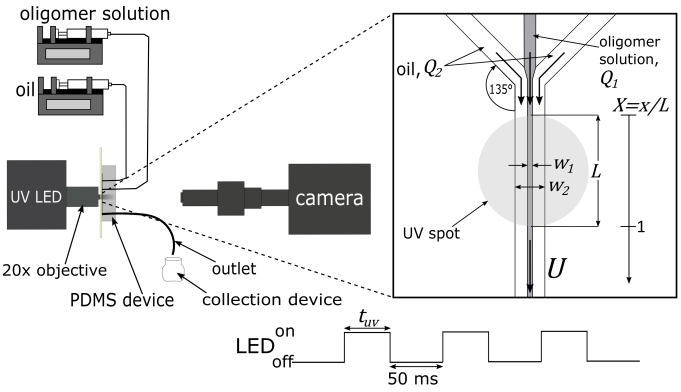

Fig. 1 Experimental set-up. Schematic diagram visualizing (left) the experimental set-up and (right) a detailed view of the focusing area of a microfluidic device, showing the uniform region of the oligomer jet flowing with speed U and the UV light spot L = 2.3 mm. The oligomer jet diameter $w_1 \approx 40$ μm, the channel width $w_2 = 200$ μm, and the flow rate ratio $Q_2/Q_1 = 7.5$. The UV LED has a pulse duration t_{uv}, and a period $= t_{uv} + 50$ ms. The dimensionless flow direction X is as indicated.

Table 1 Simplified reaction scheme for free radical photopolymerization, adapted from Decker and Jenkins[18] and Dendukuri et al.[22]

Reaction no.	Description	Reaction
I	photolysis	$P_i \xrightarrow[k_d]{h\nu} \dot{R}$
II	chain initiation	$\dot{R} + M \rightarrow R\dot{M}$
III	propagation	$R\dot{M}_n + M \xrightarrow{k_p} R\dot{M}_{n+1}$
IV	termination*	$R\dot{M}_n + R\dot{M}_m \xrightarrow{k_t} RM_{n+m}$
V	O_2 inhibition**	$\dot{X} + O_2 \xrightarrow{k_o} X\dot{O}_2$

* Only bimolecular termination reactions are considered in this work.
** $\dot{X}$ can be $\dot{R}$, $R\dot{M}$ or $R\dot{M}_n$.

oligomer solution, which can change in the flow direction (x), is denoted $M(x)$ and upstream of the region of light has constant concentration M_0. Similarly, the oxygen concentration is denoted $\theta(x)$, with upstream value θ_0. When the solution is exposed to light ($0 \le x \le L$), radicals, concentration $R(x)$, are formed at a rate r_a, which depends on the photoinitiator concentration $P_i(x)$ according to $r_a = k_d P_i$; when exposed to light the photoinitiator gives rise to radicals (reaction I), which in turn are eliminated by reacting with oxygen (reaction V) or each other, but drive polymerization by reacting with the oligomer (reaction II) thus forming the gel. For polymerization to occur, the rate of propagation has to be comparable to or greater than the rate of inhibition, thus most of the oxygen must be consumed by reacting with initiator radicals (reaction V) before reactions II and III can proceed appreciably.[18,20] Outside of the region of light, $k_d = 0$, and none of the photoinitiator is converted to radicals.

For the reactions in Table 1, at steady state the photoinitiator, radical, double bond, and oxygen concentrations vary, respectively, as

$$U\frac{dP_i}{dx} = -k_d P_i \quad \text{with} \quad P_i(0) = P_{i0}, \tag{1a}$$

$$U\frac{dR}{dx} = r_a - k_t R^2 - k_o R\theta \quad \text{with} \quad R(0) = 0, \tag{1b}$$

$$U\frac{dM}{dx} = -k_p MR \quad \text{with} \quad M(0) = M_0, \tag{1c}$$

$$U\frac{d\theta}{dx} = -k_o \theta R \quad \text{with} \quad \theta(0) = \theta_0, \tag{1d}$$

where k_d, k_t, k_p and k_o are rate constants, and typical values of the experimental parameters are given in Table 2. Below we assume that the rate constants have typical values such that $k_p \ll k_t \ll k_o$,[22] which are consistent with the values in Table 2, but the initial steps in the analysis given are more general. Also, for the range of intensities investigated in this study, 10^{-3} s$^{-1} \le k_d \le 10^{-2}$ s^{-1}. A standard approximation is that gelation occurs when $M/M_0 = 0.98$, i.e., 2 % of the double bonds are reacted.[22]

We remark that for our experimental conditions, oxygen diffusion does not contribute significantly to the oxygen concentration in the jet during UV exposure. In particular, we can compare a diffusion length $\sqrt{Dt}$ during the exposure time $t = \frac{L}{U}$ to the diameter of the jet w_1 to find $\left(\frac{DL}{Uw_1^2}\right)^{\frac{1}{2}}$, where the diffusivity of oxygen in the oligomer solution $D \sim 10^{-10}$ m^2/s.[20] This ratio is much smaller than 1, i.e., at the lowest speeds investigated, oxygen diffuses approximately 3 μm into the 40 μm diameter jet. Since the contribution is relatively small, we can simplify the model by neglecting oxygen diffusion.

We will solve these equations to determine the chemical and flow conditions that determine gelation. This solution will first consider the region of light, $k_d \ne 0$, $0 \le x \le L$, and then the downstream region where there is no light, $k_d = 0$.

3.1 Solution of the equations: Relating the oxygen, double bond and radical concentrations

First, taking the ratio of equations (1c) and (1d) yields

$$\frac{d\ln M}{d\ln\theta} = \frac{k_p}{k_o} \quad \text{with} \quad M(0) = M_0 \quad \text{and} \quad \theta(0) = \theta_0. \tag{2}$$

The solution of this equation is

$$\frac{\theta(x)}{\theta_0} = \left(\frac{M(x)}{M_0}\right)^{k_o/k_p}. \tag{3}$$

Second, we consider the equation (1b) for the evolution of the concentration of radicals $R(x)$. From equation (1a) we observe that

$$P_i(x) = P_{i0} e^{-xk_d/U}. \tag{4}$$

Hence, the radical concentration evolves according to

$$U\frac{dR}{dx} = k_d P_{i0} e^{-xk_d/U} - k_t R^2 - k_o R\theta \quad \text{with} \quad R(0) = 0. \tag{5}$$

This equation for the radical concentration is coupled with the equation for the oxygen concentration. It is convenient to nondi-

Table 2 Typical experimental values in the mathematical model of photopolymerization in flow.

Parameter	Symbol	Value	Units	Source
UV spot size	L	2.3×10^{-3}	m	measured
Average oligomer speed	U	$3.5 \times 10^{-2} - 0.11$	m/s	calculated
UV light intensity [a]	I	$1.3 \times 10^{-3} - 3.5 \times 10^{-2}$	E/(m^2 s)	measured
Initial photoinitiator concentration	P_{i0}	$131 - 787$	mol/m^3	measured
Molar extinction coefficient of photoinitiator	ε	1.6	m^3/(mol m)	Lecamp et al.[31]
Quantum yield of formation of primary radicals	φ	0.6		Dendukuri et al.[22]
Rate constant, photolysis	$k_d = \varphi\varepsilon I$	$1.3 \times 10^{-3} - 3.4 \times 10^{-2}$	s^{-1}	calculated
Rate constant, propagation [b]	k_p	10	m^3/(mol s)	Anseth et al.,[32] Beuermann et al.[33]
Rate constant, termination [b]	k_t	$10^3 - 10^4$	m^3/(mol s)	Anseth et al.,[32] Beuermann et al.[33]
Rate constant, O_2 inhibition	k_o	5×10^5	m^3/(mol s)	Decker and Jenkins[18]
Equilibrium concentration of O_2 in oligomer	θ_0	1	mol/m^3	Decker and Jenkins[18]

[a] Depth variations in UV intensity are neglected in this study; the intensity is assumed to be constant and equal to I, a measured quantity. [b] Typical order of magnitudes of the rate constants for neat acrylates, specifically di(ethylene glycol) diacrylate[32] and n-dodecyl acrylate,[33] at low conversions, approximately 2% double bonds reacted.

mensionalize the equations using

$$X = \frac{x}{L}, \qquad \Theta = \frac{\theta}{\theta_0} \quad \text{and} \quad \mathscr{R} = \frac{R}{R_c} = \frac{R}{k_d P_{i0}/(k_o\theta_0)}, \tag{6}$$

where the scale for the typical radical concentration R_c is representative of the early times (small R) when the first and last terms on the right-hand side of equation (5) approximately balance. Thus, we solve the ODEs:

$$\frac{d\mathscr{R}}{dX} = \frac{Lk_o\theta_0}{U}\left(e^{-Lk_dX/U} - \Theta\mathscr{R}\right) - \frac{Lk_dk_tP_{i0}}{Uk_0\theta_0}\mathscr{R}^2 \quad \text{for } 0 \le X < 1, \tag{7a}$$

$$\frac{d\mathscr{R}}{dX} = -\frac{Lk_o\theta_0}{U}\Theta\mathscr{R} - \frac{Lk_dk_tP_{i0}}{Uk_0\theta_0}\mathscr{R}^2 \qquad \text{for } X > 1, \tag{7b}$$

$$\frac{d\Theta}{dX} = -\frac{Lk_d}{U}\frac{P_{i0}}{\theta_0}\Theta\mathscr{R}, \tag{7c}$$

with $R(0) = 0$ and $\Theta(0) = 1$. Here we have recognized distinct equations for the region exposed to light, $0 \le X < 1$, where radicals are generated, and region downstream of light, $X > 1$, where radicals are eliminated by radical-oxygen and radical-radical combinations. In addition, the double bond concentration, rescaled as $\mathscr{M} = M/M_0$, evolves according to

$$\frac{d\mathscr{M}}{dX} = -\frac{Lk_d}{U}\frac{k_pP_{i0}}{k_0\theta_0}\mathscr{M}\mathscr{R}, \tag{8}$$

with $\mathscr{M}(0) = 1$.

In these equations we recognize several dimensionless ratios, here organized to recognize the importance of experimentally controllable parameters such as U, L and P_{i0}, while isolating the various kinetic parameters, which are typically fixed for a given experimental system. Thus, there are five dimensionless ratios that characterize the dynamics: $U/(Lk_o\theta_0)$, P_{i0}/θ_0, $k_d/(k_o\theta_0)$, k_t/k_o and k_p/k_o (note that there are alternative ways to present these ratios).

To illustrate typical trends, we first numerically solve for the evolution of the oxygen, radical and double bond concentration distributions as a function of X both within and beyond the region of light by choosing conditions that result in "high" (Figure 2) and "low" (Figure 3) oxygen concentrations. In Figure 2, we show results that illustrate how along the flow direction the oxygen concentration monotonically decreases until $X = 1$, after which it remains unchanged (the mathematical model does not include diffusion). In contrast the radical concentration increases rapidly at the start of the UV light spot, then continues to increase more gradually until $X = 1$, where it decreases rapidly to zero. The double bond concentration remains effectively unchanged since the oxygen concentration remains relatively high, approximately 85% of its initial concentration, and so the double bonds are unable to react appreciably (refer to equation (3)). Thus, no gelation or fiber formation occurs at these conditions.

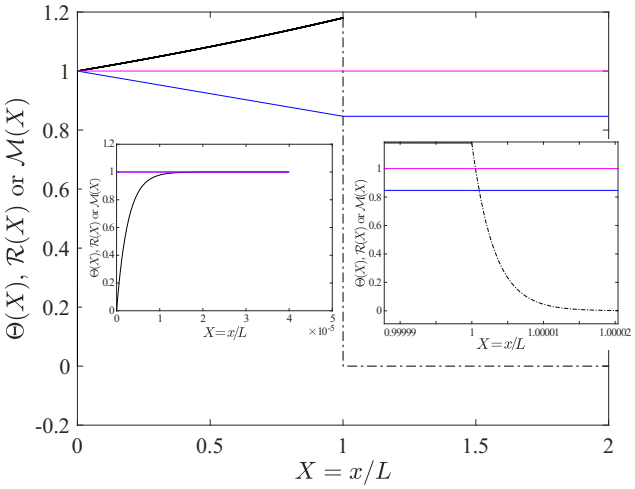

Fig. 2 Numerical simulation illustrating the "high oxygen" conditions. The main panel shows the evolution with downstream distance of the radical concentration $\mathscr{R}(X)$ (black), oxygen concentration $\Theta(X)$ (blue) and double bond concentration $\mathscr{M}(X)$ (magenta). The left inset panel illustrates the rapid change of the radical concentration near $X = 0$ where light is first applied. The right inset panel illustrates the rapid change of the radical concentration for $X > 1$, which is the region where there is no light. The oxygen concentration remains high throughout. The parameters are those of Table 2 with $U = 0.003$ m/s, $k_d = 10^{-3}$ s^{-1}, $k_t = 10^3$ m^3/(mol s), and $P_{i0} = 200$ mol/m^3.

We anticipate gelation to occur when the oxygen concentration is sufficiently small, which we expect to occur for higher

This journal is © The Royal Society of Chemistry [year]

light intensity (or higher k_d) where more photons are provided per time to increase the rate of initiator radical generation, and higher photoinitiator concentration that also leads to more radical formation per time. We test this hypothesis by increasing k_d by a factor of five and doubling P_{i0} (relative to the values used to produce Figure 2). The results for these "low" oxygen conditions are shown in Figure 3. Similar to the "high" oxygen condition, the oxygen concentration monotonically decreases, though here, decreases to zero in the light spot. The radical concentration shows the same initial rapid increase, followed by a more gradual increase, then a second rapid increase that coincides with the location at which the oxygen concentration has decreased almost to zero (note the change in scale compared to Figure 2). In addition, at this value of X, the double bond concentration starts to decrease monotonically, stabilizing at $\mathscr{M} < 0.98$. Thus for these conditions, we expect gelation and fiber formation.

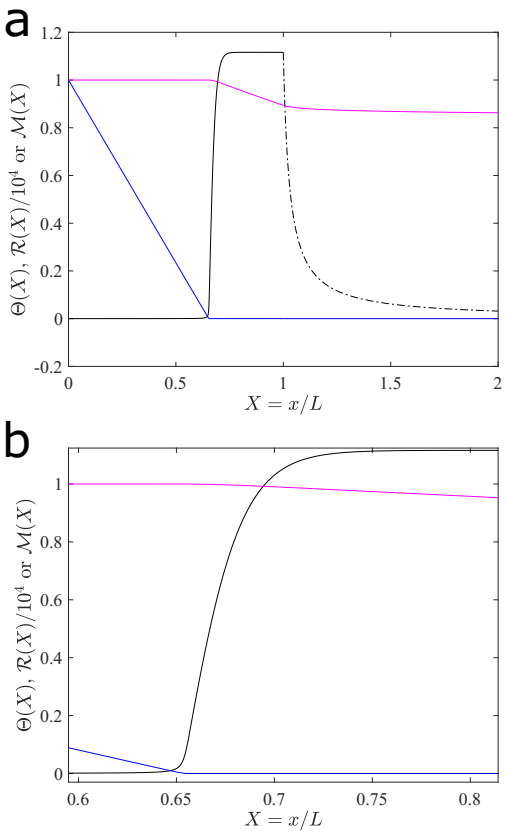

Fig. 3 Numerical simulation illustrating the "low oxygen" conditions. a. The evolution with downstream distance of the radical concentration $\mathscr{R}(X)$ (black and scaled by 10^4), oxygen concentration $\Theta(X)$ (blue) and double bond concentration $\mathscr{M}(X)$ (magenta). The oxygen concentration reaches values close to zero near $X = 0.6$ beyond which the radical concentration increases rapidly and the monomer concentration begins to decrease, which is indicative of polymerization. Beyond $X = 1$, where there is no light, the radical concentration decreases rapidly and the monomer concentration stabilizes at $\mathscr{M} \approx 0.86$. **b** displays a magnified view of the concentration profiles about $X = 0.7$, near the onset of gelation. The parameters are those of Table 2 with $U = 0.003$ m/s, $k_d = 5 \times 10^{-3}$ s^{-1}, $k_t = 10^3$ m^3/(mol s), and $P_{i0} = 400$ mol/m^3.

We next consider the typical trends in oxygen concentration when the speed is changed, while maintaining the same geometry (L) and chemical parameters. We expect smaller flow speeds (for the same chemistry) to yield lower oxygen concentrations as the reacting fluid is exposed to light for a longer time. In Figure 4, we report results corresponding to changing the speed from large values, for which little reaction is possible (oxygen concentrations stay relatively large), to smaller values, where the speed is sufficiently slow that most of the oxygen is consumed in the region of light $X < 1$; in this latter limit we would expect gelation, as discussed above. In particular, we see that for smaller speeds the oxygen can readily be consumed for $X < 1$. In Section 4, we probe these kinds of ideas experimentally.

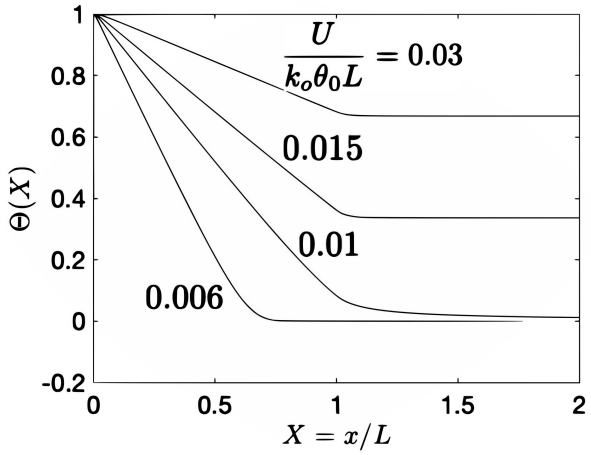

Fig. 4 Numerical solution for the evolution of the oxygen $\Theta(X)$ for different speeds. With increasing speed, more oxygen is present at a given position X. The parameters are $U/(k_o\theta_0 L) = 0.006, 0.01, 0.015, 0.03$, $k_t/k_o = 0.01$, $k_d/(k_o\theta_0) = 0.0001$, and $P_{i0}/\theta_0 = 100$.

3.2 Approximate solution of the equations: Radical and oxygen concentrations

From equation (7a), we neglect the last term (radical-radical termination) and combine with equation (7c) to arrive at

$$\frac{d}{dX}\left(R - \frac{k_o\theta_0^2}{k_d P_{i0}}\Theta\right) = \frac{Lk_o\theta_0}{U}e^{-Lk_dX/U} \tag{9}$$

with $R(0) = 0$ and $\Theta(0) = 1$. We integrate (9) and apply the initial conditions to find (with some rearrangement)

$$R(X) + \frac{k_o\theta_0^2}{k_d P_{i0}}(1 - \Theta(X)) = \frac{k_o\theta_0}{k_d}\left(1 - e^{-Lk_dX/U}\right) \tag{10}$$

or

$$\frac{k_d P_{i0}}{k_o\theta 0^2}R(X) - \Theta(X) + 1 = \frac{P_{i0}}{\theta_0}\left(1 - e^{-Lk_dX/U}\right). \tag{11}$$

Since $\frac{k_d P_{i0}}{k_0\theta_0^2} \ll 1$, this leads to the approximate solution

$$\Theta(X) \approx \frac{P_{i0}}{\theta_0}\left(e^{-XLk_d/U} - 1\right) + 1. \tag{12}$$

Also, since $Lk_d/U \ll 1$, we can simplify the exponential term to find

$$\Theta(X) \approx 1 - \frac{Lk_d P_{i0}X}{U\theta_0}. \tag{13}$$

This linear variation in oxygen concentration is evident in the numerical solutions shown in Figure 4.

We expect polymerization to occur when $\Theta \ll 1$, which means that the maximum speed U_c to still achieve gelation by the end of the region of light exposure $X = 1$ is $U_c \leq Lk_dP_{i0}/\theta_0$. In these limits, if speeds are faster, then the fluid does not pick up sufficient light to achieve the necessary polymerization. Alternatively, we can conclude that these critical conditions correspond to higher allowed critical speeds for higher initial concentrations of photoinitiator.

In contrast, for "lower" speeds, where the photoinitiator concentration decays exponentially, then starting with equation (12), $\Theta \approx 0$ leads to a critical speed U_c (above which we expect no polymerization) versus photoinitiator relation:

$$U_c \approx -\frac{Lk_d}{\ln(1-\theta_0/P_{i0})}. \tag{14}$$

For $\theta_0/P_{i0} \ll 1$, then again

$$U_c \approx \frac{Lk_dP_{i0}}{\theta_0}. \tag{15}$$

We will test this prediction of a critical speed for effective gelation in the experiments described in Section 4.2.

4 Results and Discussion

In the experiments, four main conditions were manipulated in order to control fiber production: oligomer flow rate Q_1 (while maintaining $Q_2/Q_1 = 7.5$), UV light intensity I, pulse duration t_{uv}, and initial photoinitiator concentration P_{i0}. Q_1 controls the UV exposure time of the oligomer solution as it flows past the UV spot. In the experimental set-up (Figure 1), the maximum exposure time t_L of a fluid element is the time it takes to flow the entire illuminated distance L. For the purpose of this discussion, intensity and exposure time, which is inversely proportional to Q_1, will often be grouped together under the term *energy* (energy/area $\propto I/Q_1$). Furthermore, I, Q_1 and P_{i0} all directly influence the concentration of initiator radicals produced in the oligomer jet upon exposure to UV light. The number density of initiator radicals determines whether solid fibers form, and if solid fibers are produced, the concentration of initiator radicals will affect the flexibility and length of these fibers.

4.1 Qualitative characterization of fiber production

Variations of I, Q_1 and P_{i0} yielded three distinct regimes of fiber production, as shown in Figure 5. The first regime is characterized by no fiber production, and is observed at conditions that generate relatively low concentrations of initiator radicals, for example, insufficient P_{i0} and/or energy. In addition, samples collected within this regime do not have any observable areas of polymerized or partially-polymerized material. This observation suggests that at these conditions, insufficient radicals are produced to scavenge the dissolved oxygen in the oligomer jet (equations (1b), (1d)), which prevents polymerization and the formation of solid (gel) fibers. These observations are consistent with the "high oxygen" conditions considered numerically in Section 3.1 and Figure 2.

At some critical condition of P_{i0} and energy, which will be discussed in the following section, we observe a second regime of fiber production that is characterized by the production of nonuniform fibers. As shown in Figure 5a, these fibers do not all meet our desired product criteria: uniform straight cylindrical fibers with diameters comparable to the jet diameter. The energy and P_{i0} conditions are sufficient for solidification since fibers or fiber-like objects are produced, but are not sufficient for uniform fiber production. Unlike the first regime, enough radicals are produced to scavenge most of the dissolved oxygen, such that the rate of inhibition (reaction V in Table 1) is comparable to or less than the rate of chain initiation and propagation (reactions II, III). Gelation can occur at these conditions, but the number density of reacted double bonds in the fibers is low, which limits the shape fidelity and mechanical properties of the resulting product. This transitional regime of fiber production is distinguished by the presence of semi-polymerized blobs, fiber-like objects that have abnormal shapes, such as irregular kinks, crimped regions or are attached to larger polymerized areas, and fibers that are extremely thin, when compared to the diameter of the oligomer jet (the smaller solid object size relative to the liquid template dimensions observed at "low" polymerization conditions, such as those used to produce the fibers shown in Figure 5a, has been reported previously for photopolymerized microspheres, and attributed to oxygen diffusion[23]). In addition, these experiments are expected to produce one fiber for every pulse, but trials within this transitional regime often yielded significantly fewer fibers than expected.

The third regime of fiber production is characterized by the production of uniform fibers (Figure 5b,c). The system is not limited by P_{i0} or energy, and the produced fibers exhibit a uniform straight cylindrical shape along the majority of their length. The only nonuniformities are found at the beginning and end of each fiber, which are areas that were exposed to UV light for less time than the majority of the fiber's length. As a result, the extrema of uniform fibers are softer and thinner, often tapering to a point or ending in a bifurcation. Additionally, in these samples, no semi-polymerized blobs are observed, the fibers do not exhibit large amounts of tangles or knots, and the expected amount of fibers, based on the pulse frequency and duration, are produced.

The lower extreme of the uniform fiber regime, with respect to the amount of P_{i0} and energy required, produces relatively soft and deformable fibers. These lower-extreme fibers are noticeably curved and may include areas of crimp along their lengths (Figure 5b). Some of these fibers include segments that appear straight and are connected by large bends or irregular shapes. As the concentration of P_{i0} and energy increases, more rigid fibers are produced (Figure 5c). They are relatively straight, and any noticeable curvature is distributed along the entire length of the fibers. These fibers are up to 30% larger in diameter than those produced in the second regime (Figure 5a) and are less susceptible to bending when agitated. At the highest P_{i0} and energy conditions investigated in this study, extremely brittle fibers are produced that do not bend appreciably and are prone to breaking.

This journal is © The Royal Society of Chemistry [year]

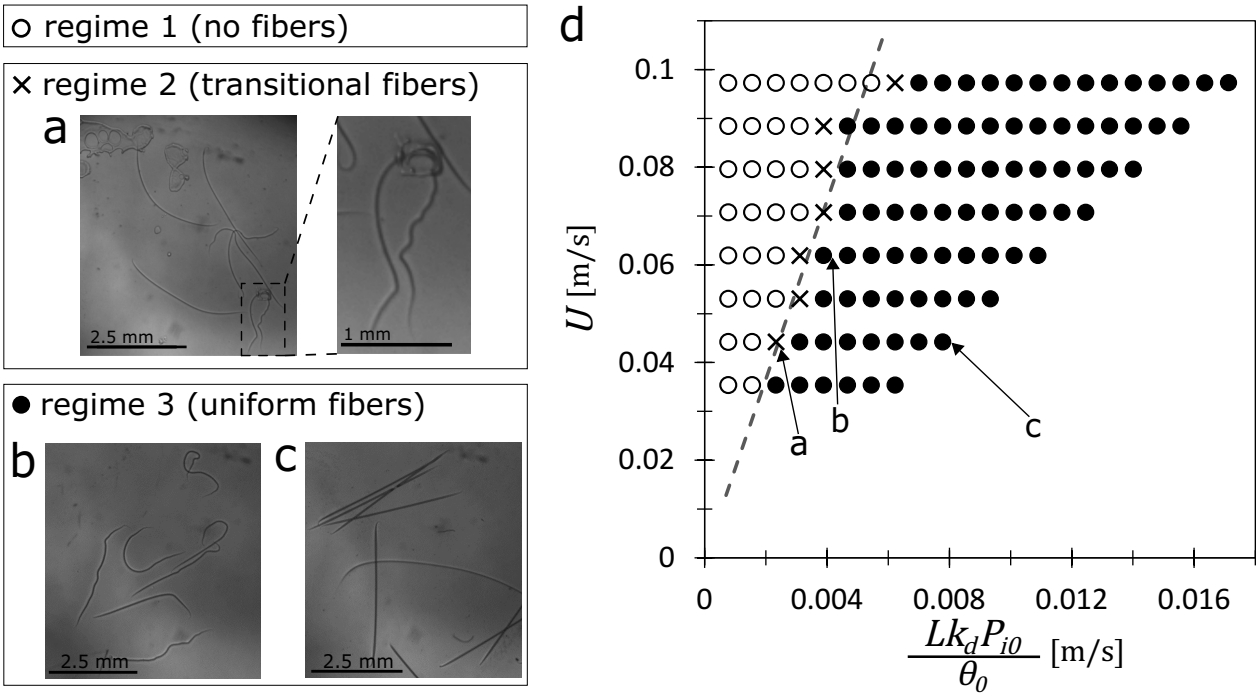

Fig. 5 Regimes of fiber production. a-c. Representative images of **(a)** transitional fibers produced in regime 2, with an enlarged view of a single transitional fiber, **(b)** relatively soft uniform fibers produced in regime 3, and **(c)** relatively rigid uniform fibers produced in regime 3 (more rigid than those in **b**). **d.** Regime diagram for fiber production in terms of the oligomer speed U and $\frac{Lk_dP_{i0}}{\theta_0}$ indicating no observations of fibers production (regime 1), the production of transitional or non-uniform fibers (regime 2), and uniform fiber production (regime 3). The dashed line, a linear fit through the transitional values with a slope ~ 18, indicates the critical conditions for fiber production; to the left of the line, on average no fibers are produced, and to the right, reproducible fiber production is observed. The conditions used to produce the fibers shown in **a**-**c** are indicated on the regime diagram.

The observations for the second and third regimes of fiber production are consistent with the "low oxygen" numerical solutions discussed in Section 3.1 and Figure 3, where the oxygen concentration decreases almost to zero before the fluid exits the UV spot. For these conditions, sufficient double bond conversion is achieved to gel the flowing oligomer solution, and the greater the degree of conversion of double bonds, the more rigid the resulting fiber. The production regimes are summarized in the diagram shown in Figure 5d, where increased rigidity and/or uniformity are observed for higher photoinitiator concentrations, higher intensities and lower flow rates (higher energy), i.e., towards the lower right of the regime diagram.

4.2 Critical conditions for fiber formation

The critical conditions for fiber formation, or in other words, the conditions for the transition from the first to second regime of fiber production (Figure 5a), can be determined by systematically increasing I in fixed increments until fibers are observed for a range of Q_1 values; in this case the photoinitiator concentration $P_{i0} = 262$ mol/m^3. These observations are shown in Figure 5d, where the oligomer speed U, calculated from Q_1 is represented on the vertical axis. I is shown on the horizontal axis in terms of the ratio $\frac{Lk_dP_{i0}}{\theta_0}$ (or $\frac{L\varphi\varepsilon IP_{i0}}{\theta_0}$), with units of speed; we use literature values of φ, ε, and θ_0 as reported in Table 2. We observe that as the flow speed of the oligomer jet U increases, the minimum UV intensity I_c at which solid fibers are produced (shown as $\times$'s in Figure 5d) also increases approximately linearly. This trend is expected from the approximate solution of the steady-state flow model (equation (15)).

Experimentally, we find that multiple flow rates correspond to the same I_c, which we refer to as a "stack" of flow rates. This observation may be attributed to the 0.0013 E/(m^2 s) increment of intensity between trials, which limits our ability to resolve more precisely the critical conditions for fiber production. The actual I_c for fiber production is likely lower than represented in Figure 5d, especially for the lower flow rates in the "stack". The lowermost speed in a "stack" of speeds corresponding to a single critical light intensity can be assumed to produce the most crosslinked fibers in the "stack" because those fibers were exposed to UV light of the same intensity for a longer time than those produced at the higher flow speeds in the "stack".

Figure 5d and equation (15) indicate an inverse relationship between I_c and P_{i0}. After substituting for $k_d = \varphi\varepsilon I$, equation (15) can be rearranged to

$$I_c \approx \frac{U_c\theta_0}{\varepsilon\varphi LP_{i0}}. \tag{16}$$

To demonstrate this relationship more clearly, we plot the critical intensity as a function of photoinitiator concentration maintaining a constant flow rate, as shown in Figure 6. We observe that there is a roughly linear relationship between I_c and $\frac{1}{P_{i0}}$, consistent with equation (16), indicating that as P_{i0} increases, the critical intensity for fiber formation decreases. The experimental data displayed in Figures 5d and 6 show good qualitative agreement with the approximate model prediction (equation 15),

however the model predicts a critical speed that is a factor ~ 18 lower than observed. Since we can produce solid fibers at significantly higher speeds than predicted, it means that we are consuming oxygen and/or forming radicals and/or propagating radicals faster than accounted for in the construction of our model. There are several factors that may contribute to this difference. For example, a few of our simplification steps rely on our understanding of the relative magnitudes of the rate constants (k_p, k_t, and k_o), values that we obtain from the scientific literature for related neat monomer systems, and not the specific oligomer solution composition used in this work. It is possible that there may be significant differences, for example, others have shown that there can be a significant enhancement of the polymerization rates, factor of ten or more, of hydrophilic monomers in water due to hydrogen bonding and other stabilizing interactions.[34] Furthermore, we assume that oxygen is consumed by reaction V (Table 1) only. However, it is observed that at very early times during the delay or inhibition period in quiescent gelation, oxygen can be consumed in a chain peroxidation process, where as many as eight oxygen molecules are consumed by one initiator radical.[18] The oligomer solution also contains an acrylated rhodamine B dye (1 mol/m^3), which contains both secondary and tertiary amine groups that can potentially form radicals that consume oxygen in chain peroxidation or can react with acrylate monomers to reinitiate polymerization.[18,35]

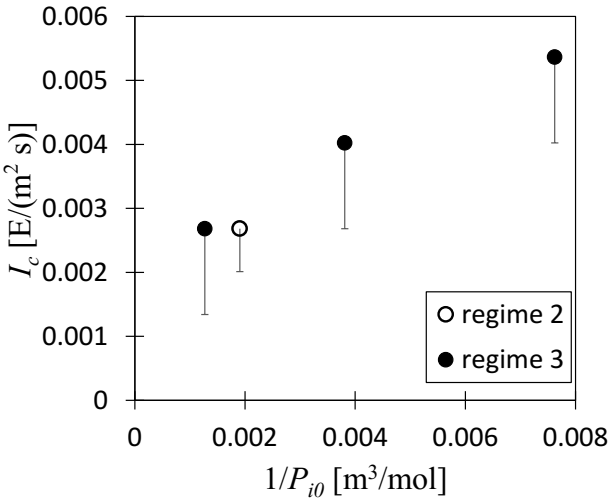

Fig. 6 Critical intensity for fiber formation as a function of inverse photoinitiator concentration. The minimum intensity observed to produce fibers at a fixed flow rate $Q_1 = 0.16$ ml/h, where error bars represent the intensity increment (maximum error bound) used in this study, except for the transitional fiber observation (regime 2), where the error is half of the intensity increment.

4.3 Factors influencing fiber length

We can vary the experimental conditions (Q_1, I, t_{uv} and P_{i0}) to directly and predictably affect fiber length. Furthermore, if we assume the volume of the oligomer jet is conserved during gelation, we can estimate the length of fiber that will be produced as a function of the oligomer flow rate and the pulse duration. Given that the average velocity in the jet U can be obtained by dividing Q_1 by the cross-sectional area of the cylindrical oligomer jet of diameter w_1, we estimate the length of liquid exposed to UV light during a pulse, $l_1 = Ut_{uv}$. The calculation of l_1 assumes that the entire exposed length of the oligomer jet has flowed past the same illuminated distance (corresponding to the same exposure time along the entire length), and that this distance is sufficient to absorb the light energy required to gel. For example, this illuminated distance can be the maximum illuminated distance L, which corresponds to an exposure time t_L. However, this assumption does not account for the possibility that at the instant the light turns on (or off), the fluid already in the UV spot that has flowed an illuminated distance $< L$ may have absorbed at least the minimum amount of energy needed to gel. Thus, we define a second length $l_2 = l_1 + L$, which acknowledges that some of the oligomer solution in the UV spot at the beginning and end of a pulse may contribute to the fiber length.

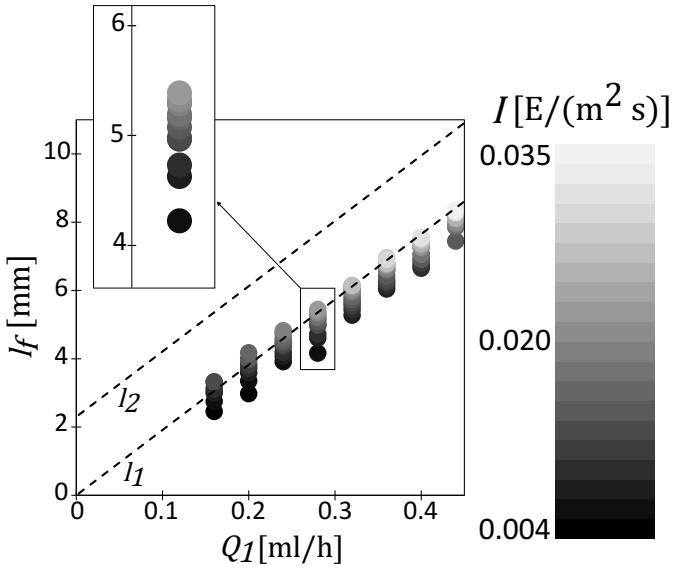

Fig. 7 Effect of oligomer flow rate on fiber length. Intensity I is indicated using a gradient scale, with low intensities corresponding to dark points on the graph, and high intensities corresponding to light points on the graph. The lower and upper dashed lines represent calculated fiber lengths l_1 and l_2, respectively. The interval of I tested for Q_1 = 0.16 ml/h spanned from 0.0042 - 0.011 E/(m^2 s), increasing in regular intervals of 0.0013 E/(m^2 s). For further trials, the upper bound was increased proportionally to Q_1. All trials were executed with t_{uv} = 100 ms. The inset is an enlarged view of the data from the $Q_1 = 0.28$ ml/h trials, highlighting the large separation between the three lowermost points that represent fibers within the transitional regime of fiber production, and the rest of the stack. Error bars for fiber length are smaller than the data points used in the figure.

As expected, the measured fiber length l_f increases with increasing Q_1, as shown in Figure 7. l_1 and l_2, which characterize the fiber fabrication process in terms of a predicted range of fiber lengths, are represented by the two dashed lines on the graph; they exhibit the same linear relationship with Q_1, with the only difference being that l_2 is displaced upwards by L. For each flow rate investigated, we systematically increased intensity in regular intervals, which resulted in increases in the fiber length. This data is represented in the "stacks" for each Q_1 shown in Figure 7. Most

This journal is © The Royal Society of Chemistry [year]

of the data in the l_f "stacks" represent fibers produced in the third regime of fiber production, i.e., uniform fibers (Figure 5b,c), except for the lowermost points, which represent transitional fibers (Figure 5a).

When l_f is directly proportional to Q_1 (data points on, or parallel to, l_1 or l_2 in Figure 7), the oligomer jets absorb comparable amounts of light energy. The intensities required to produce fibers with $l_f \approx l_1$ at different flow rates were compared, and we observe that I is a linear function of Q_1, which supports the qualitative observation of similar rigidity (Figure S1†). Also, the slope $(\Delta I/\Delta Q_1)$ increases as relative fiber length, fiber rigidity and the degree of polymerization increases (recall, energy/area $\propto I/Q_1$). Larger slopes, i.e., greater energy, yield longer fibers because there is more energy for the extremities of the oligomer passing partially through the UV spot to be polymerized. For fibers to be created with length l_2, a very large I would be required to polymerize the extremities of the jet—the lengths of oligomer exposed to UV light for very small amounts of time—and we expect the majority of these lengths would be extremely rigid. Therefore, the higher a fiber length relative to the range $l_1 - l_2$ in Figure 7, the higher its degree of polymerization and rigidity, so the difference between l_f and l_1 (or l_2) provides a means of characterizing a fiber's relative degree of polymerization and rigidity.

To further characterize the effect of intensity on fiber length, we focus on the data in each l_f "stack" in Figure 7, and find that the data (l_f as a function of I) can be fit to a power law, where the fractional power law exponent decreases with increasing Q_1 (Figure S2†). Thus, as Q_1 increases, the equivalent increase in intensity does not have a significant effect on l_f or fiber rigidity. This property can be observed where the lengths of the fibers created at large values of Q_1 are concentrated within a smaller "stack". Even though these fibers were created over a comparatively greater interval of I than the fibers produced at small values of Q_1, they exhibit a much less pronounced change in l_f (Figure S3†). In addition, as Q_1 increases, the three regimes of fiber production spread out over disproportionately large intervals of I.

The lowermost points of each l_f "stack" in Figure 7 are often greatly displaced from the other data points for a given Q_1 (see Figure 7 inset). In particular, the lowermost three points, displaced from the majority of the data for a given Q_1, represent fibers produced within the transitional regime (Figure 5a). This observation suggests that fibers within the transitional regime of fiber production experience greater changes in their properties, including length and rigidity, due to minimal adjustments to the conditions of their production. Because the transitional regime of fiber production is observed for a relatively small range of Q_1 and I compared to the regime where no fibers are produced and the uniform fiber regime, yet spans a large range of properties with respect to shape, dimensions and rigidity, it follows that any changes to the fabrication conditions within this regime would have large effects on the properties of the produced fibers.

The effect of pulse duration t_{uv} on fiber length was also investigated. Keeping I and Q_1 constant, we decreased t_{uv} from 300 ms to 5 ms, and observed that l_f decreases linearly except as t_{uv} approaches 0 ms, as seen in Figure 8a. In the inset, highlighting values of t_{uv} close to 0, the two dashed lines represent l_1, where the lower line corresponds to Q_1 = 0.16 ml/h and $I = 0.011$ E/(m^2 s), and the upper line corresponds to a higher Q_1 = 0.48 ml/h and $I = 0.032$ E/(m^2 s). These two lines both approach 0 as pulse duration approaches 0, while the fiber length l_f approaches small, non-zero values as t_{uv} approaches 0. This discrepancy leads to the estimate l_1 becoming increasingly inaccurate as the pulse duration becomes very small.

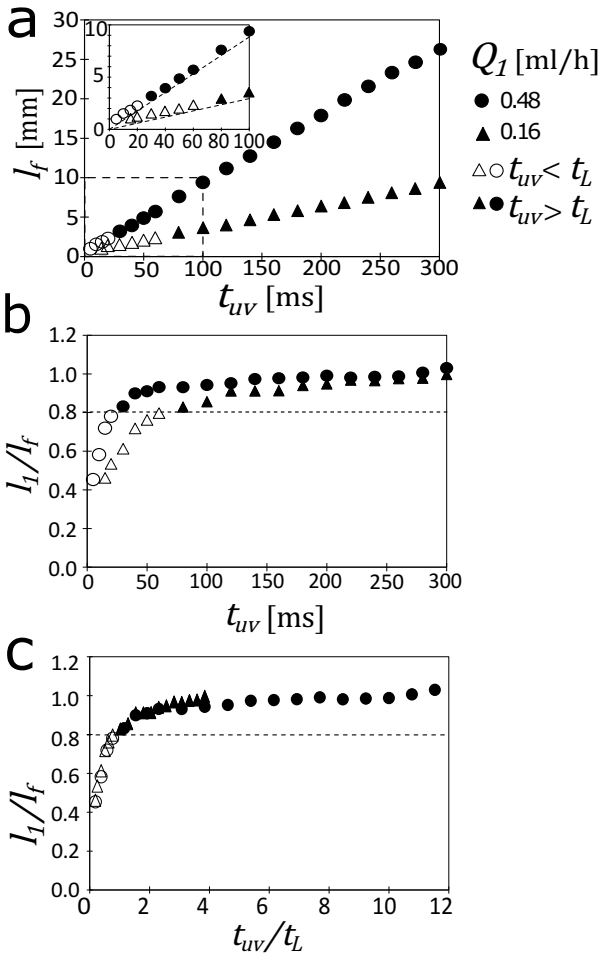

Fig. 8 Effect of pulse duration on fiber length. a. The relationship between t_{uv} and l_f, displayed for Q_1 = 0.16 and 0.48 ml/h; I = 0.011 and 0.032 E/(m^2 s), respectively. Included in the upper left inset is a magnified view of the relationship between pulse duration and fiber length at pulse times approaching 0 ms. **b.** The relationship between the ratio l_1/l_f and pulse duration. **c.** l_1/l_f plotted as a function of t_{uv}/t_L, collapsing the data onto a single curve. The dotted lines in **b** and **c** represent the approximate transition point in the trends of the curves. Open data markers represent fiber lengths from trials in which the time necessary for fluid to flow across the UV spot t_L is greater than the pulse duration t_{uv}. Error bars for fiber length are smaller than the data points used in the figure.

The discrepancy between l_f and l_1 at low t_{uv} can be more clearly observed when the ratio l_1/l_f is plotted against pulse duration, t_{uv}, as shown in Figure 8b. When $t_{uv} > t_L$, l_1/l_f is relatively constant and approaches a value of 1 for both high and low Q_1; in this range, the majority of the polymerized material in the fiber experiences the same exposure time $= t_L$ independent of the pulse duration, which, for the data shown in Figure 8, is more than suf-

ficient for gelation. The fiber length contributions from exposure times $< t_L$ (at the beginning and end of the pulse) are relatively small for these long fibers. As t_{uv} decreases, the ratio l_1/l_f decreases gradually and then experiences a sharp decrease when t_L becomes greater than t_{uv}. We note that, at $t_{uv} = t_L$, the measured fiber length is slightly larger than the UV spot size, and this difference is comparable to the extrapolated intercepts in Figure 8a ($\approx 0.5 - 0.6$ mm). When the pulse duration approaches 0 and $t_{uv} < t_L$, the fluid cannot flow the entire UV spot length L during a single pulse, so the maximum exposure time is instead $= t_{uv}$, and the major contribution to the fiber length is no longer l_1. Therefore, while l_1 decreases linearly with shorter pulses, the measured fiber length deviates increasingly from this estimate, where there is a constant offset: $l_f - l_1 \approx 0.5$ mm for $t_{uv}/t_L \leq 1$.

We also report the data l_1/l_f as a function of the normalized time t_{uv}/t_L. In this representation of the data (Figure 8c), both curves from Figure 8b collapse onto a single curve, i.e. the curves for all possible Q_1 will stack on top of each other. In addition, the lowest points in the collapsed curves, representing the conditions at which any further decrease in pulse duration would no longer yield fibers, are located at the same ratio of length l_1/l_f and time t_{uv}/t_L. This result suggests that there is a critical point at which fibers can no longer be produced in our system, and that this point can be quantified using the ratio l_1/l_f or t_{uv}/t_L.

Fiber length also depends on P_{i0} and I, as shown in Figure 9. When P_{i0} is low, changes in intensity yield large changes in l_f, as noted in Figure 9a. However, when P_{i0} is increased, identical changes in I do not produce comparable changes in l_f. There is a positive, nonlinear relationship between P_{i0} and l_f (Figure 9a). When P_{i0} is low, increasing P_{i0} yields large changes in l_f. However, at larger values of P_{i0}, the same increase in P_{i0} can have a minimal effect on l_f. Therefore, Figure 9a supports the previous statement that fibers within the transitional regime experience large changes in properties with minimal adjustments to the conditions of their production. The small change to P_{i0} between 131 mol/m^3 and 262 mol/m^3, with the majority of the 131 mol/m^3 fibers lying within the transitional regime, led to a large difference in l_f, while subsequent greater variations in P_{i0}, occurring within the uniform regime of fiber production, did not have a comparable effect on fiber length.

When the fiber length is plotted as a function of the product of I and P_{i0} (Figure 9b), all of the data for trials spanning from the first fibers produced in the transitional regime to fibers produced well within the uniform regime of fiber production approximately fall on the same curve. The dotted line on this plot represents l_1 for the given Q_1 and t_{uv}, kept constant throughout all experiments included in Figure 9. The product of I and P_{i0} is proportional to the rate of production of primary radicals r_a in the oligomer jet when exposed to UV light, so this result indicates that the fiber length is dependent on the concentration of initiator radicals produced.

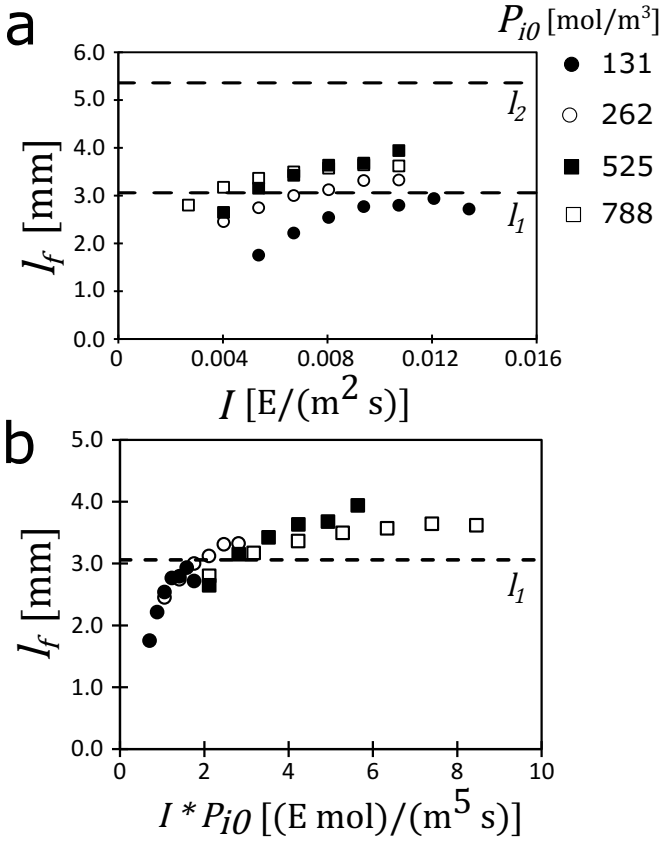

Fig. 9 Effect of intensity and photoinitiator concentration on fiber length. a. The relationship between the intensity and measured fiber length for different photoinitiator concentrations. **b.** The relationship between the product of intensity and photoinitiator concentration and measured fiber length. The trials were executed with $Q_1 = 0.16$ ml/h and $t_{uv} =$ 100 ms. Error bars for fiber length are smaller than the data points used in the figure.

5 Conclusions

In this work, we present the quantitative relationships between the length of fibers produced through continuous-flow gelation and their conditions of production, most notably photoinitiator concentration, intensity of the UV spot, and oligomer flow rate. This paper also works to establish three regimes of fiber production, in which (1) fibers are not produced, (2) fibers are produced with irregular shape, notable deformities, semi-polymerized blob material, and/or in a significantly smaller quantity that expected, and (3) regularly shaped fibers are produced, with no obvious deformities and in the expected quantity. Characterization of these production regimes, along with the relationships between the fiber length and processing conditions, can be used to develop reproducible guidelines for standardized fiber production for a broad range of experimental conditions. We have also qualitatively observed and compared the rigidity of the microfibers produced with these conditions. Future studies can employ flow deformation techniques[36–39] that have been developed to quantify modulus. Such characterizations may serve as a useful starting point in designing fibers with controlled spatial modulus heterogeneities along the fiber length using intensity moduluation during a single pulse.

In addition, we developed a steady-state flow model for the oxygen-inhibited photopolymerization process that allows for a better understanding of the chemical processes involved during continuous flow gelation by connecting the chemistry to the flow

This journal is © The Royal Society of Chemistry [year]

conditions. The model captures the correct trend in the relationship among the process parameters—flow rate, intensity, and photoinitiator concentration—for the critical conditions for fiber formation. However, quantitatively it predicts slower gelation conditions than observed experimentally. While we believe our model takes a considerable step in capturing the flow gelation process, a better understanding of the complex and multi-step kinetics involved in free-radical gelation is important. In particular, though the experimental determination of rate constants can be challenging, it is important for future model development.

For simplicity, we neglect oxygen diffusion in this model, which is reasonable for the experimental conditions considered. However, for conditions where this approximation is not valid, such as the polymerization of thin or submicron jets, the model will require the construction and solution of partial differential equations. Looking ahead, it will also be useful to compare to flow gelation systems with significantly reduced oxygen inhibition.[35] Another interesting avenue for future work will be exploring both experimentally and theoretically the impact of the velocity profile on the gelation kinetics, which is not considered in this paper but may become a significant factor in high viscosity ratio systems.

Acknowledgements

We thank Joel Nunes for assistance with building the fiber fabrication set-up. We also thank Roman Akhmechet and the PRISM cleanroom (Princeton University) for assistance with mold fabrication. This work is supported by NSF Grant CMMI-1661672 and the Materials Research Science and Engineering Center supported by NSF Grant DMR 1420541.

References

1 E. Kang, G. S. Jeong, Y. Y. Choi, K. H. Lee, A. Khademhosseini and S.-H. Lee, *Nat. Mater.*, 2011, **10**, 877–883.

2 Y. Yu, H. Wen, J. Ma, S. Lykkemark, H. Xu and J. Qin, *Adv. Mater.*, 2014, **26**, 2494–2499.

3 P. Xu, R. Xie, Y. Liu, G. Luo, M. Ding and Q. Liang, *Adv. Mater.*, 2017, **29**, 1701664.

4 Y. Liu, K. Zhang, J. Ma and G. J. Vancso, *ACS Appl. Mater. Interfaces*, 2017, **9**, 901–908.

5 S. Nakajima, R. Kawano and H. Onoe, *Soft Matter*, 2017, **13**, 3710–3719.

6 E. Um, J. K. Nunes, T. Pico and H. A. Stone, *J. Mater. Chem. B*, 2014, **2**, 7866–7871.

7 H. Onoe, T. Okitsu, A. Itou, M. Kato-Negishi, R. Gojo, D. Kiriya, K. Sato, S. Miura, S. Iwanaga, K. Kuribayashi-Shigetomi, Y. T. Matsunaga, Y. Shimoyama and S. Takeuchi, *Nat. Mater.*, 2013, **12**, 584–590.

8 Y. Yu, L. Shang, W. Gao, Z. Zhao, H. Wang and Y. Zhao, *Angew. Chem. Int. Ed.*, 2017, **56**, 12127–12131.

9 A. Perazzo, J. K. Nunes, S. Guido and H. A. Stone, *Proc. Natl. Acad. Sci. U.S.A.*, 2017, **114**, E8557–E8564.

10 J. Cheng, Y. Jun, J. Qin and S.-H. Lee, *Biomaterials*, 2017, **114**, 121 – 143.

11 M. A. Daniele, D. A. Boyd, A. A. Adams and F. S. Ligler, *Adv. Healthcare Mater.*, 2015, **4**, 11–28.

12 J. K. Nunes, S. S. H. Tsai, J. Wan and H. A. Stone, *J. Phys. D: Appl. Phys.*, 2013, **46**, 114002.

13 D. Dendukuri, D. Pregibon, J. Collins, T. Hatton and P. Doyle, *Nat. Mater.*, 2006, **5**, 365–369.

14 W. Jeong, J. Kim, S. Kim, S. Lee, G. Mensing and D. J. Beebe, *Lab Chip*, 2004, **4**, 576–580.

15 S. Xu, Z. Nie, M. Seo, P. Lewis, E. Kumacheva, H. A. Stone, P. Garstecki, D. B. Weibel, I. Gitlin and G. M. Whitesides, *Angew. Chem. Int. Ed.*, 2005, **44**, 724–728.

16 S. C. Laza, M. Polo, A. A. R. Neves, R. Cingolani, A. Camposeo and D. Pisignano, *Adv. Mater.*, 2012, **24**, 1304–1308.

17 A. J. D. Krüger, O. Bakirman, L. P. B. Guerzoni, A. Jans, D. B. Gehlen, D. Rommel, T. Haraszti, A. J. C. Kuehne and L. De Laporte, *Adv. Mater.*, 2019, **0**, 10.1002/adma.201903668.

18 C. Decker and A. D. Jenkins, *Macromolecules*, 1985, **18**, 1241–1244.

19 M. D. Goodner and C. N. Bowman, *Macromolecules*, 1999, **32**, 6552–6559.

20 A. K. O'Brien and C. N. Bowman, *Macromolecules*, 2006, **39**, 2501–2506.

21 A. Vitale, M. G. Hennessy, O. K. Matar and J. T. Cabral, *Adv. Mater.*, 2015, **27**, 6118–6124.

22 D. Dendukuri, P. Panda, R. Haghgooie, J. M. Kim, T. A. Hatton and P. S. Doyle, *Macromolecules*, 2008, **41**, 8547–8556.

23 K. Krutkramelis, B. Xia and J. Oakey, *Lab Chip*, 2016, **16**, 1457–1465.

24 Y. Zhang, C.-F. Wang, L. Chen, S. Chen and A. J. Ryan, *Adv. Funct. Mater.*, 2015, **25**, 7253–7262.

25 K. J. Lee, J. Yoon, S. Rahmani, S. Hwang, S. Bhaskar, S. Mitragotri and J. Lahann, *Proc. Natl. Acad. Sci. U.S.A.*, 2012, **109**, 16057–16062.

26 J. K. Nunes, K. Sadlej, J. I. Tam and H. A. Stone, *Lab Chip*, 2012, **12**, 2301–2304.

27 R. V. Bell, C. C. Parkins, R. A. Young, C. M. Preuss, M. M. Stevens and S. A. F. Bon, *J. Mater. Chem. A*, 2016, **4**, 813–818.

28 X. Deng, Y. Ren, L. Hou, W. Liu, Y. Jia and H. Jiang, *ACS Appl. Mater. Interfaces*, 2018, **10**, 40228–40237.

29 D. Qin, Y. Xia and G. M. Whitesides, *Nat. Protoc.*, 2010, **5**, 491–502.

30 G. Odian, *Principles of Polymerization*, Wiley, New Jersey, 4th edn, 2004.

31 L. Lecamp, P. Lebaudy, B. Youssef and C. Bunel, *Polymer*, 2001, **42**, 8541 – 8547.

32 K. S. Anseth, C. M. Wang and C. N. Bowman, *Polymer*, 1994, **35**, 3243 – 3250.

33 S. Beuermann, D. A. Paquet, J. H. McMinn and R. A. Hutchinson, *Macromolecules*, 1996, **29**, 4206–4215.

34 B. De Sterck, R. Vaneerdeweg, F. Du Prez, M. Waroquier and V. Van Speybroeck, *Macromolecules*, 2010, **43**, 827–836.

35 S. C. Ligon, B. Husár, H. Wutzel, R. Holman and R. Liska, *Chem. Rev.*, 2014, **114**, 557–589.

36 J. Cappello, M. Bechert, C. Duprat, O. du Roure, F. Gallaire and A. Lindner, *Phys. Rev. Fluids*, 2019, **4**, 034202.

37 B. Marchetti, V. Raspa, A. Lindner, O. du Roure, L. Bergougnoux, E. Guazzelli and C. Duprat, *Phys. Rev. Fluids*, 2018, **3**, 104102.

38 C. Duprat, H. Berthet, J. S. Wexler, O. du Roure and A. Lindner, *Lab Chip*, 2015, **15**, 244–252.

39 M. M. Villone, J. K. Nunes, Y. Li, H. A. Stone and P. L. Maffettone, *Soft Matter*, 2019, **15**, 880–889.

This journal is © The Royal Society of Chemistry [year]